Article

How Cloud Droplet Number Concentration Impacts Liquid Water Path and Precipitation in Marine Stratocumulus Clouds—A Satellite-Based Analysis Using Explainable Machine Learning

Lukas Zipfel [1,2,*], Hendrik Andersen [1,2], Daniel Peter Grosvenor [3,4] and Jan Cermak [1,2]

1 Institute of Meteorology and Climate Research, Karlsruhe Institute of Technology (KIT), 76131 Karlsruhe, Germany; hendrik.andersen@kit.edu (H.A.); jan.cermak@kit.edu (J.C.)
2 Institute of Photogrammetry and Remote Sensing, Karlsruhe Institute of Technology (KIT), 76131 Karlsruhe, Germany
3 Met Office Hadley Centre, Exeter EX1 3PB, UK; daniel.grosvenor@metoffice.gov.uk
4 Institute for Climate and Atmospheric Science, School of Earth and Environment, University of Leeds, Leeds LS2 9JT, UK
* Correspondence: lukas.zipfel@kit.edu

Abstract: Aerosol–cloud–precipitation interactions (ACI) are a known major cause of uncertainties in simulations of the future climate. An improved understanding of the in-cloud processes accompanying ACI could help in advancing their implementation in global climate models. This is especially the case for marine stratocumulus clouds, which constitute the most common cloud type globally. In this work, a dataset composed of satellite observations and reanalysis data is used in explainable machine learning models to analyze the relationship between the cloud droplet number concentration (N_d), cloud liquid water path (LWP), and the fraction of precipitating clouds (PF) in five distinct marine stratocumulus regions. This framework makes use of Shapley additive explanation (SHAP) values, allowing to isolate the impact of N_d from other confounding factors, which proved to be very difficult in previous satellite-based studies. All regions display a decrease of PF and an increase in LWP with increasing N_d, despite marked inter-regional differences in the distribution of N_d. Polluted (high N_d) conditions are characterized by an increase of 12 gm^{-2} in LWP and a decrease of 0.13 in PF on average when compared to pristine (low N_d) conditions. The negative N_d–PF relationship is stronger in high LWP conditions, while the positive N_d–LWP relationship is amplified in precipitating clouds. These findings indicate that precipitation suppression plays an important role in MSC adjusting to aerosol-driven perturbations in N_d.

Keywords: aerosol–cloud–precipitation interactions; cloud droplet number concentration; machine learning; marine stratocumulus; remote sensing; satellite observations

1. Introduction

Marine stratocumulus clouds (MSC) are known as the most common cloud type, covering more than 20% of the global oceans in the annual mean with local coverage over subtropical and midlatitude oceans sometimes above 50% [1]. MSC have a strong impact on the Earth's radiative budget by increasing the planetary albedo, as they are brighter than the ocean surface below. Comparatively small changes in the radiative properties of such marine boundary layer clouds can, therefore, lead to large changes in global shortwave reflectivity [2,3]. Changes in cloud properties in response to aerosol emissions and climate change can, thus, lead to large uncertainties in predictions of future climate [4–6].

The cloud shortwave radiative effect (CRE_s) of MSC is dependent on the clouds' properties, such as effective droplet radius (r_e), cloud droplet number concentration (N_d),

liquid water path (LWP), and cloud fraction (CLF), which in turn depend on environmental conditions. N_d is related to the availability of aerosols, which function as cloud condensation nuclei (CCN) during cloud formation. Increases in N_d with constant liquid water will lead to a lower r_e, resulting in an increase in the CRE_s known as the Twomey effect [7]. In addition to this immediate effect on the CRE_s, subsequent effects from aerosol–cloud–precipitation interactions (ACI) through resulting cloud adjustments further alter the radiative forcing.

For polluted clouds (characterized by higher CCN), the more numerous and smaller droplets lead to subsequent LWP adjustments within the cloud through two counteracting pathways: precipitation suppression and entrainment feedback [8,9]. The initial droplet formation process in MSC through condensation of liquid water on CCN can produce droplets up to a size of ∼20 μm [1]. Further growth to droplets large enough to precipitate is realized through coalescence (the merging of cloud droplets), either by collision of multiple small droplets (termed "autoconversion" [10]) or by a larger droplet that collects smaller droplets ("accretion"). Under conditions with elevated N_d and a resulting decrease in r_e the process of collision–coalescence is inhibited due to its strong dependence on the droplet size ([1]). The subsequent decrease in precipitation is expected to lead to an increase in LWP and cloud lifetime [11] due to a less stable boundary layer and the weakened cloud liquid water sink [12]. However, the extent to which the process of precipitation suppression impacts clouds is unclear. Previous studies that use observations of natural and anthropogenic aerosol emission events to estimate the impact of indirect ACI on clouds suggest there is no or only a negligible LWP adjustment in clouds as a response to N_d perturbations [9,13], calling into question the impact of precipitation suppression on a global scale. In contrast, in a recent study, Gupta et al. [14] showed the importance of precipitation suppression in environments with elevated levels of aerosol for the Southeast Atlantic Ocean (SEA) with observation data acquired in the NASA ObseRvations of Aerosols above CLouds and their intEractionS (ORACLES) campaign [15,16]. In addition to the suppression of precipitation, the reduced droplet radius is also hypothesized to lead to a decrease in droplet sedimentation speed [17,18] and an increased evaporation–entrainment rate at the cloud top acting as a LWP sink [19–21], which is further enhanced in less stable situations with a lower humidity above the cloud top.

Accordingly, by way of the two opposing processes described above, the cloud LWP adjustment in response to N_d perturbations could potentially be positive, negative, or even absent [8]. Previous studies have shown that the LWP response to N_d perturbations is dependent on the cloud state [3,22] with findings of a stronger increase in LWP with N_d in precipitating clouds likely attributed to precipitation suppression [23]. If precipitation suppression is the dominating process through which N_d controls the LWP sinks, it is to be expected that there is a decrease in precipitation with increasing N_d. On the other hand, a decrease in LWP in non-precipitating clouds with increasing N_d may be indicative of enhanced entrainment feedback. The objective of this study is to analyze the impact of changes in N_d on precipitation and liquid water path in MSC by utilizing statistical machine learning models and data from satellite observation. While previous studies (e.g., [8,24,25]) have presented the N_d–LWP relationship using satellite data, it has proved very difficult or impossible to disentangle the impact of changes in N_d alone as a causative factor due to various other confounding factors. In this work, the use of machine learning models allows these confounding factors to be controlled for, enabling the analysis of the impact of N_d in isolation. This represents a step-change in the ability to use observations to quantify ACI effects and provides a robust metric for testing and improving climate models.

2. Materials and Methods

This study is conducted for five marine regions that each cover 10° by 10° and are characterized by a high annual occurrence of stratocumulus clouds as defined by Klein and Hartmann [26]. The regions are named according to the closest eastward coastline as displayed in Table 1. A machine learning model is fitted in each region based on a

combination of satellite observations and reanalysis model data in order to asses the impact of changes in cloud droplet number concentration (N_d) on precipitation and LWP, and factors controlling these relationships.

Table 1. Locations of the study domains with the total number of observations (N) and the explained variability for the PF (R^2_{pf}) and LWP (R^2_{lwp}) models.

Region Name	Latitude	Longitude	N	R^2_{pf}	R^2_{lwp}
Australia	25° S–35° S	95° E–105° E	16,504	0.63	0.61
California	20° N–30° N	120° W–130° W	18,919	0.71	0.65
Canaries	15° N–25° N	25° W–35° W	8431	0.65	0.67
Namibia	10° S–20° S	0°–10° E	20,337	0.68	0.66
Peru	10° S–20° S	80° W–90° W	23,512	0.63	0.66

2.1. Data

The dataset used here is a refined version of the data used in Zipfel et al. [23]. Satellite observations of various cloud properties are taken from the CALIPSO-CloudSat-CERES-MODIS Merged Release B1 (C3M) product, which is available for July 2006 to April 2011. The C3M dataset is based on the Clouds and the Earth's Radiant Energy System (CERES) with a resolution of ~20 km [27]. Observations from multiple additional sensors (Cloud-Aerosol Lidar and Infrared Pathfinder Satellite Observation (CALIPSO), Cloudsat, and Moderate Resolution Imaging Spectroradiometer (MODIS)) are collocated for each of these CERES "footprints". A footprint, therefore, represents an individual observation with data from all four instruments combined. Each CERES footprint is further segmented into a maximum of 16 cloud groups (distinguished as unique entities as seen from above) and up to 6 cloud layers (distinguished vertically) by utilizing the high resolution and vertical profiles provided by CALIPSO and CloudSat.

Only CERES footprints with a single cloud layer are used in this study to exclude the influence of superimposing clouds. Additionally only observations of low-level clouds are selected by limiting the cloud top height (CTH) to 3 km [28]. CTH is defined as the median of all cloud groups in a CERES footprint.

To analyze the impact of the cloud droplet number concentration on precipitation formation, the CloudSat precipitation flag is used to calculate the precipitation fraction (PF). The precipitation flag consists of four possible classes (no precipitation, liquid, solid, or drizzle) and provides this classification for each cloud group. The PF is calculated for each CERES footprint and is defined as the number of cloud groups where any form of precipitation is detected by CloudSat, divided by the total number of cloud groups [23]. Drizzle is the prevalent class of precipitation detected over all regions (>88% of precipitating cloud groups). Only a total of two observations of solid precipitation are found in the Peru region.

Using MODIS retrievals of the effective cloud-droplet radius (r_e), the cloud optical depth (τ_c), the cloud-top temperature, and the cloud-top pressure, the cloud-droplet number concentration (N_d) is calculated according to Grosvenor et al. [29]:

$$N_d = \frac{\sqrt{5}}{2\pi k} \sqrt{\frac{f_{ad}\, c_w\, \tau_c}{Q_{ext}\, \rho_w\, r_e^5}} \tag{1}$$

where $k = 0.8$, $f_{ad} = 0.66$, and $Q_{ext} = 2$. While the overall uncertainty in the calculated N_d is estimated to amount to around 78% at the native MODIS resolution of 1 km^2 [29], this is likely reduced for the footprint averages utilized here. The accuracy of the N_d calculation was further improved by utilizing the r_e and the τ_c provided by the CERES enhanced cloud algorithm. The enhanced cloud algorithm makes use of the CALIPSO and CloudSat cloud height and cloud mask retrievals in addition to the MODIS reflectances to obtain r_e and τ_c [27], reducing the number of cases where default values for observations outside the lookup table are used in the standard CERES algorithm. Furthermore, any instances where

r_e or τ_c are below 4 are removed from the dataset due to the associated uncertainties for retrievals in this range [30]. Finally, only the 1st–99th percentiles for N_d are used in order to remove any remaining outliers possibly introduced by measurement errors.

Information on the background environment is provided to the model through the meteorological reanalysis data taken from the ERA5 dataset available through the European Centre for Medium-Range Weather Forecasts (ECMWF) at a 0.25° × 0.25° resolution on an hourly basis [31,32]. Data for mean sea-level pressure (MSL), sea-surface temperature (SST), air temperature, relative humidity (RH), u, and vs. wind components and vertical velocity are collocated with the C3M data. The pressure levels in the ERA5 data that are closest to the lower and upper cloud boundaries are then chosen based on the cloud-base height (CBH) and CTH from CALIPSO. For each CERES footprint, these pressure levels are then used to select the temperature, RH and wind components below the cloud, and the RH and wind components above the cloud (Table 2). Additionally, the 2 m air temperature and the temperature at 700 hPa from ERA5 are used to calculate the estimated inversion strenght (EIS) according to Wood and Bretherton [33], assuming a surface pressure of 1010 hPa.

Table 2. Overview of the variables used in the machine learning models.

Variable Name	Abbreviation	Origin
Temperature below cloud	T_{bc}	ERA5
Vertical velocity below cloud	w_{bc}	ERA5
Winds below cloud	u_{bc}/v_{bc}	ERA5
Winds above cloud	u_{ac}/v_{ac}	ERA5
Relative humidity below cloud	RH_{bc}	ERA5
Relative humidity above cloud	RH_{ac}	ERA5
Mean sea level pressure	MSL	ERA5
Sea surface temperature	SST	ERA5
Estimated inversion strength	EIS	ERA5
Cloud top height	CTH	CALIPSO
Precipitation fraction	PF	CloudSat
Cloud droplet number concentration	N_d	MODIS
Liquid water path	LWP	AMSR-E
Rain water content [1]	RWC	AMSR-E

[1] RWC not used to predict LWP.

The liquid water path (LWP) and the rain water content (RWC) are obtained from the Level-2B precipitation product Version 3 of the Advanced Microwave Scanning Radiometer-Earth Observing System (AMSR-E) sensor aboard the Aqua satellite. To avoid the risk of an introduction of a pseudo-relationship in the N_d and LWP retrievals due to correlated errors when both are based on the MODIS sensor, the AMSR-E product is utilized as an independent source of LWP measurement. The data are provided with a resolution of 5 km across track and 10 km along track [34]. To maintain a similar spatial scale for all satellite observations, the mean LWP and the mean RWC is calculated for each CERES footprint based on the five AMSR-E pixels closest to the center of that footprint as in [23].

2.2. Models

Gradient Boosting Regression Tree (GBRT) models are trained to predict PF and LWP in all regions. GBRTs are able to capture non-linear relationships while considering the interaction effects between the predictor parameters, and do not depend on the input data having a specific distribution [35]. GBRT and other tree based machine learning models have been utilized to analyse low-level clouds and ACI in the past [23,36–39]. The input variables for the machine learning models are displayed in Table 2. The PF model utilizes all variables as input features, while the LWP model does not use the RWC. This was done to reduce the impact of confounding errors in those models, as both LWP and RWC are retrieved from the AMSR-E sensor, which is known to have problems separating LWP and RWC especially in situations with low amounts of liquid water [40]. Shapley additive

explanation (SHAP) values are calculated for each individual model and used to analyze the effect of changes in N_d on the predicted cloud parameters (PF and LWP).

SHAP values quantify the contribution of each predictor variable (model feature) to the model prediction [41,42]. The sign of a feature's SHAP value corresponds to a decrease (negative SHAP value) or increase (positive SHAP value) the model prediction (relative to the mean prediction value) in response to a feature's observed value. Therefore, each model prediction for an individual observation can be described as the sum of the mean model prediction (defined as the mean of the predictand variable provided to the model for training) and the SHAP values for all model features related to that observation. The SHAP values themselves are the sum of the main effects, which are attributed to a single feature (the current main feature) and the interaction effects which account for the impact of the corresponding secondary features. Interaction effects can be analyzed to explore the relationship between multiple model features and their impact on the model prediction. They are defined as the change in the SHAP value of the main feature that occurs when the secondary feature is removed.

Prior to the analysis of the GBRT models' SHAP values, hyperparameter tuning was performed to optimize the explained variability (R^2, Table 1) and minimize the Root Mean Squared Error (RMSE) by utilizing a training and a test dataset, which, respectively, had 70% and 30% of the data assigned randomly. The hyperparameters for the models have been adjusted following a grid search of three parameters that have the strongest impact on model performance (learning rate = 0.05, number of estimators = 1000, maximum tree depth = 3). Additionally, the minimum number of samples per leaf was set to 50 to help prevent the models from overfitting.

3. Results

An overview of the five study regions and the spatial distribution of the grid cell averages for N_d, PF, and LWP is shown in Figure 1. All regions display a gradient from the east (closer to the coastline) towards the open ocean in the west with decreasing N_d and increasing PF and LWP, indicating a negative relationship of N_d with PF and LWP. This gradient is less pronounced for the Canaries and the Australian region (Figure 1b,c), likely due to the larger distance to the coast and the prevailing wind direction resulting in a reduced influence of continental aerosol emissions. The continental influence is also evident from the maxima in observed N_d, which are highest in the Californian and Namibian region (indicated by the dark brown shading, Figure 1a,c), while the Canaries and the Australian region show markedly lower N_d maxima (light brown shading, Figure 1b,c). In the following Sections 3.1 and 3.2, the N_d–PF (N_d–LWP) relationship is analyzed using machine learning, specifically exploring the influence of LWP (PF).

3.1. Precipitation Fraction

The regional machine learning models are able to explain 63–71% of the observed variability in PF (R^2 shown in Table 1) in the independent test data, displaying a similar performance across the different regions. Figure 2 shows the SHAP values for N_d (N_d–SHAP) for the models predicting PF across the five regions. Each dot represents a single observation and is colored by LWP. All five regions are characterized by a decrease in predicted PF with increasing N_d (Figure 2a–e). This negative relationship is characterized by a steep decrease in N_d–SHAP for the lower spectrum of the N_d distribution (approximately 0–200 droplets cm^{-3}), which then stagnates at higher N_d. Therefore, increases in N_d above $\sim$200 cm^{-3} do not lead to a further substantial decrease in PF.
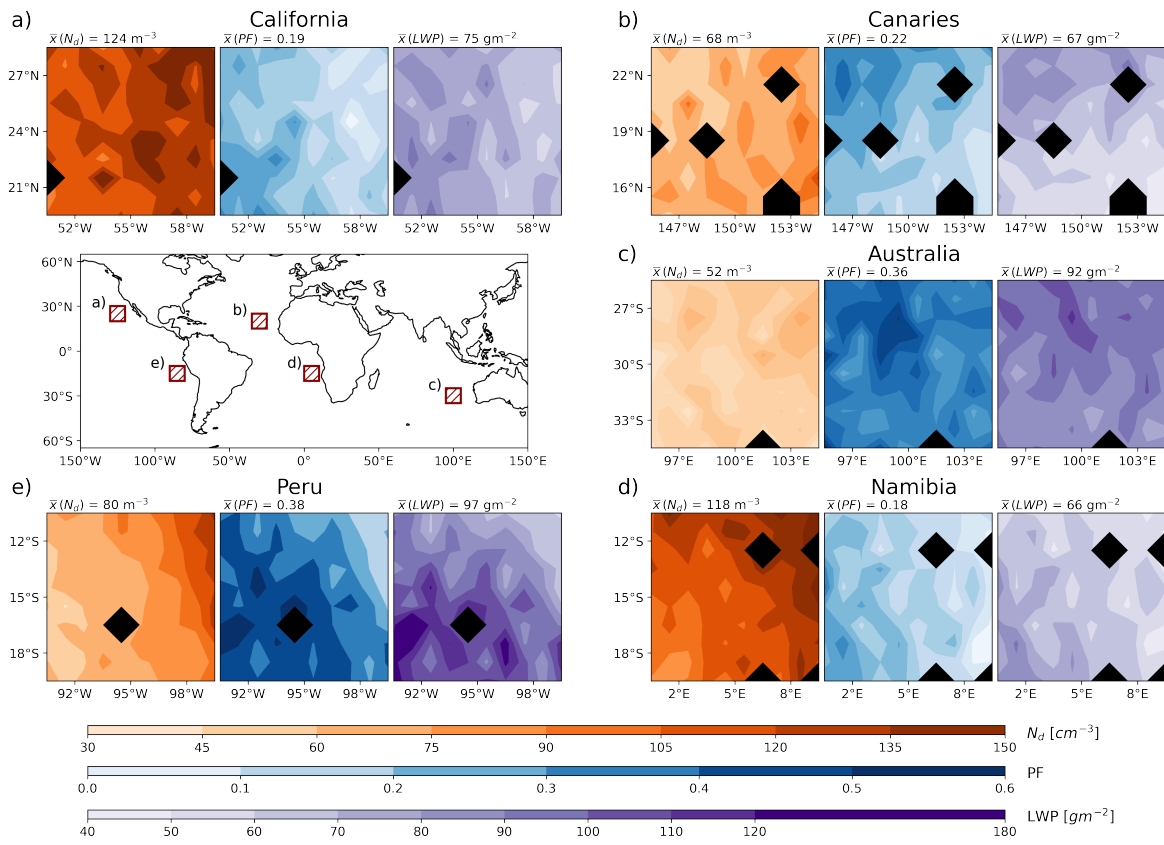
Figure 1. Overview of the five regions analyzed in this study. Contour plots (**a**–**e**) show the grid cell mean N_d (brown shading), PF (blue shading), and LWP (purple shading) for each region based on data aggregated on a 1° by 1° grid for the years of 2006–2011. Grid cells with less than five observations are shown in black. Regional averages are displayed above the contour plots. For reference, each region (**a**–**e**) is additionally displayed as a red rectangle in the global map.
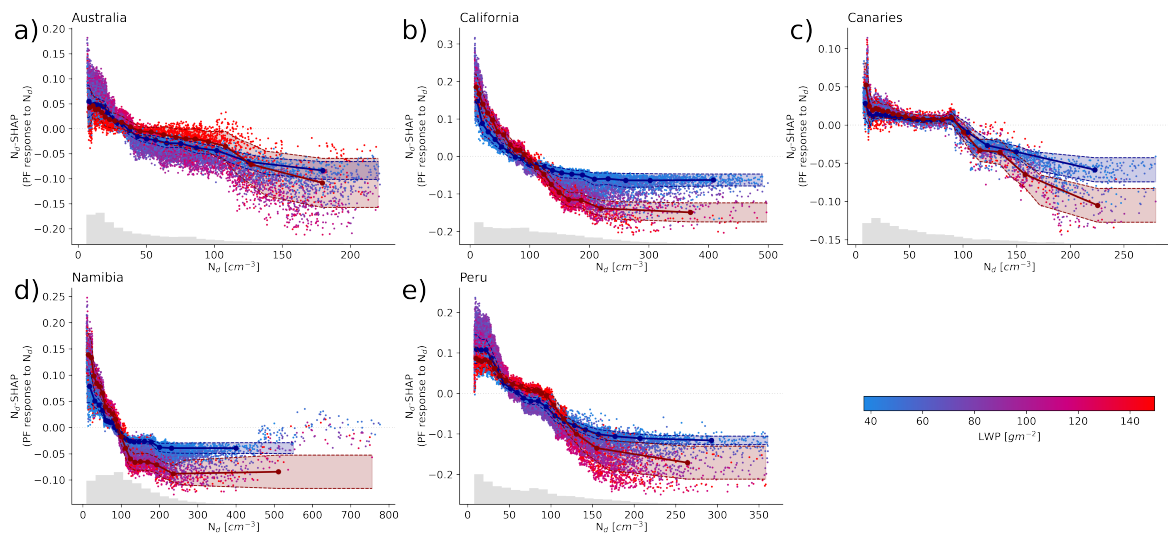

Figure 2. Scatter plots for the five stratocumulus regions (**a**–**e**) showing the effect of changes in N_d on PF using SHAP values. Each dot represents a single observation. The LWP for each observation is indicated by color increasing from blue to red. The interconnected dots show the median N_d–SHAP value for 20 equal sample bins across N_d for the 1st (blue) and 4th (red) LWP quartiles with one standard deviation indicated by the shaded areas. Shown in grey at the bottom of each panel is a histogram of the distribution of observed N_d.

To analyze the impact of LWP as a secondary model feature on the N_d–SHAP, we compare the observations based on the 1st and 4th quartile of LWP. The average LWP for the lower quartile is close to 40 gm^{-2} for all regions, while the average LWP for the upper quartile is $\sim$160 gm^{-2} for the Australian and Peruvian region and in the range of 120–130 gm^{-2} for the Canaries as well as the Californian and Namibian region. In order to better display the predicted PF response to possible interactions with LWP, the lower and upper LWP quartiles are split into 20 equal N_d sample bins (ESB). The interconnected dots in Figure 2 show the median N_d–SHAP value of the ESB, with shading indicating one standard deviation. The ESB lines are colored according to their respective LWP quartile (lower quartile—blue, upper quartile—red). In all regions, with the exception of Australia (Figure 2b–e), there is a discernible difference in the predicted PF response to N_d between the low (blue) and high (red) LWP cases, suggesting an amplified sensitivity of PF to N_d in high-LWP environments and a dampened N_d–PF sensitivity for below-average LWP.

To test whether these observed differences in N_d–PF sensitivity are actually attributed to LWP in the machine learning model, interaction effects are analyzed. The interaction effects for N_d and LWP are depicted in Figure 3 and colored by LWP. Here, the interaction effects are defined as the change in the PF response to an N_d value when LWP is present as a model predictor versus a model without LWP. Therefore, it quantifies how sensitive the predicted PF response to N_d is to the secondary feature LWP. The interaction effects clearly show a separation of the PF response to N_d by LWP. In low LWP conditions (blue dots), interaction effects tend to increase with N_d, whereas the opposite is the case for high LWP conditions (red dots), which becomes especially apparent in the diverging pattern for $N_d > 100$. This shows that in the machine learning model, the predicted PF response to N_d is modulated by LWP where the negative N_d–PF sensitivity is amplified in high LWP conditions (adding the negative N_d–LWP interaction effect relationship to the negative N_d–PF relationship), but dampened in low LWP conditions (adding the positive N_d–LWP interaction effect relationship to the negative N_d–PF relationship). In the Californian, Canarian, Namibian, and Peruvian region (Figure 3b–e), observations characterized by a high LWP show a negative impact on the predicted PF as opposed to observations with a low LWP. This suggests that in the machine learning model the differences in N_d–PF sensitivity for high and low LWP situations are in fact caused by LWP. The distinction between high and low LWP cases is not as clear for the Australian region, however (Figure 2a). Similarly, in Figure 3a, the LWP interaction effects on N_d–SHAP are not as clearly separable for low and high LWP cases as for the other regions. This may be attributed to the lack of high N_d observations in the region.
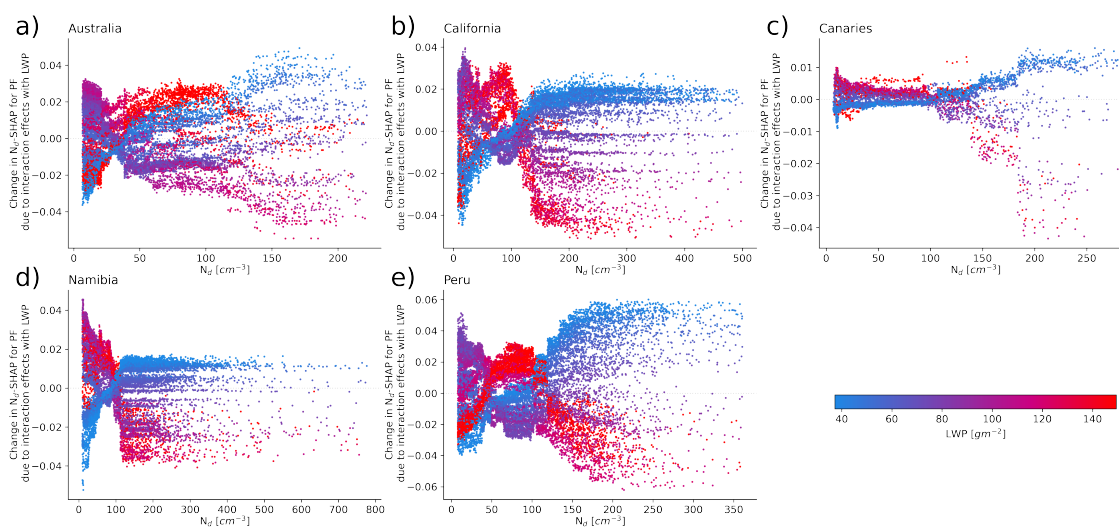

Figure 3. Scatter plots for the five stratocumulus regions (**a–e**) showing the interaction effects for N_d and LWP when predicting PF. Each dot represents a single observation. The LWP is indicated by color increasing from blue to red.

To quantify the N_d–PF relationship and enable an inter-regional comparison despite marked differences in the N_d distribution, two distinct N_d bins are defined: (i) pristine conditions where $20 < N_d < 50$ and (ii) polluted conditions where $150 < N_d < 250$. The sensitivity of PF (S_{PF}) to changes in N_d is then defined as the difference in the median SHAP value of the polluted bin minus the pristine bin. To assess the impact of the LWP control on the N_d–PF relationship suggested above (Figures 2 and 3), the 1st and 4th quartile of LWP are used to calculate S_{PF} for low (S_{PF}^l) and high (S_{PF}^h) LWP conditions, respectively. S_{PF} values for all regions are displayed in Figure 4 with color indicating the LWP conditions. All five regions are characterized by a negative S_{PF} with an inter-regional average of -0.13. A negative S_{PF} indicates a decrease of the predicted PF with increasing N_d that is attributed solely to N_d. As SHAP values are always given in units of the model's predictions, they have the advantage of simplifying the interpretation of the physical impact of S_{PF}. Accordingly, a S_{PF} of -0.13 refers to an N_d-driven median reduction of PF by 13 percentage points from pristine to polluted conditions (e.g., a median PF of 0.40 in pristine and 0.27 in polluted conditions). Throughout all five regions, high LWP conditions display a stronger negative N_d–PF sensitivity ($S_{PF}^h < S_{PF}^l$), with an inter-regional average S_{PF}^h of -0.16, compared to an average S_{PF}^l of -0.10. The Californian ($S_{PF}^h = -0.22$, $S_{PF}^l = -0.11$) and Namibian ($S_h = -0.16$, $S_l = -0.08$) regions show the largest differences in sensitivities, with S_{PF}^h values twice as large as S_{PF}^l.
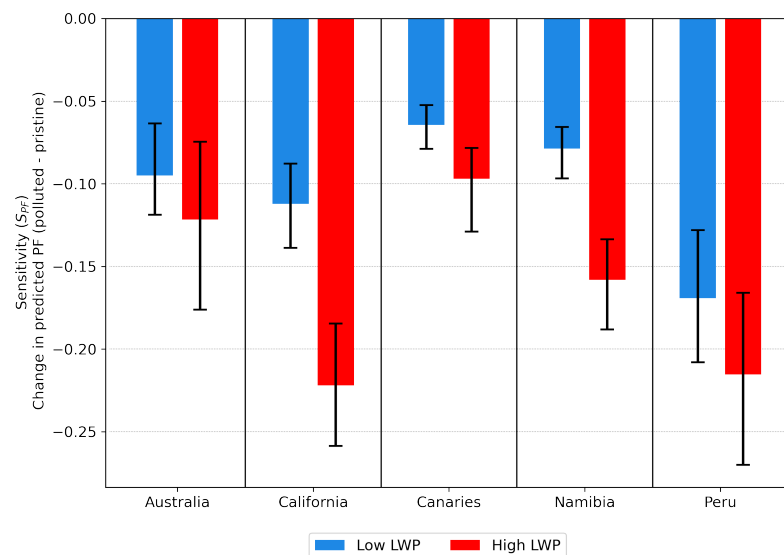

Figure 4. Sensitivity of PF (S_{PF}) to changes in N_d defined as the difference in the bin median Nd-SHAP values between the $20 < N_d < 50$ and $150 < N_d < 250$ bins. Error bars show the range of the differences between the 25th and the 75th percentile of both N_d bins. Values are shown for both low LWP (S_{PF}^l, blue) and high LWP (S_{PF}^h, red) conditions.

3.2. Liquid Water Path

Similar to the previous section, the machine learning models predict LWP equally well across the five regions with an explained variability in the range of 61–67% (Table 1) in the independent test data. Figure 5 shows the SHAP values for N_d for the models predicting LWP akin to Figure 2, but with each dot colored by PF. The models for all regions show a positive N_d–LWP relationship (Figure 5a–e) as the SHAP values increase with higher N_d. The increase in predicted LWP is larger at low N_d values, whereas at higher N_d (i.e., $N_d > 100$), LWP is less sensitive to further increases in droplet number, which has been shown for the Namibian stratocumulus region in previous work [23]. This saturation effect is consistent across all regions except the Canaries, where the predicted LWP is shown to increase with N_d even for $N_d > 100$. Aside from the Canaries, the saturation effect seems to be independent of the large inter-regional differences observed in the distribution of N_d.

It is worth noting that the Californian and Peruvian regions (Figure 5b,e) display a slight decrease in LWP in high N_d conditions for non-precipitating clouds (blue dots), which may be indicative of entrainment feedback.
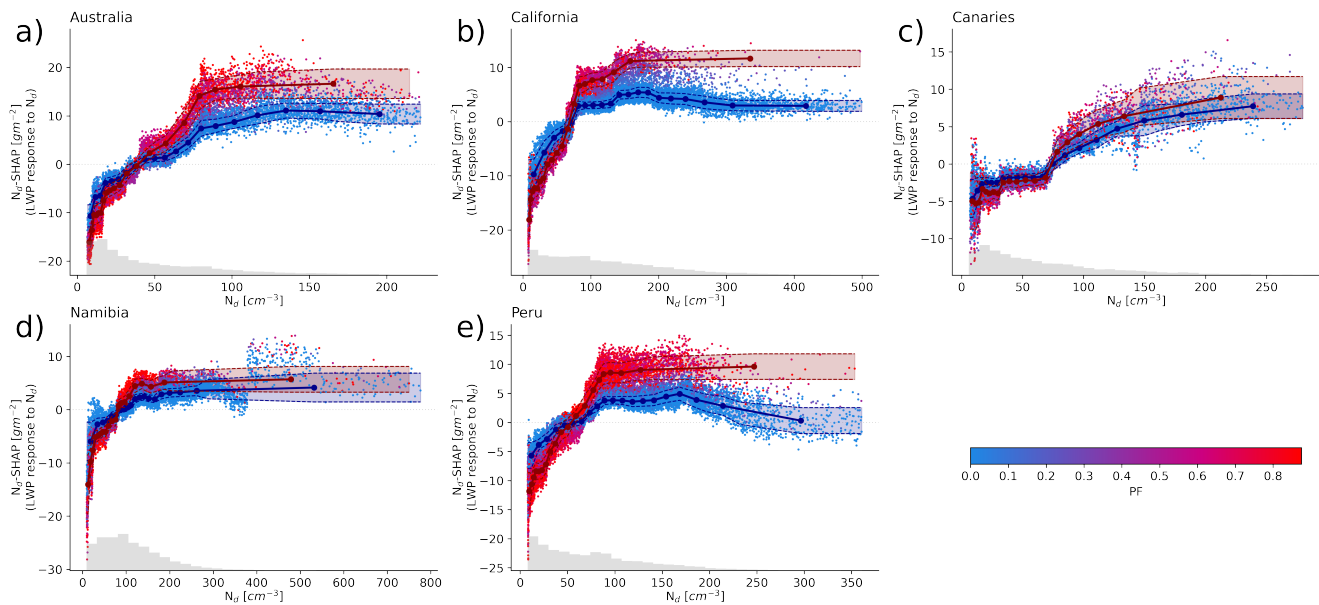

Figure 5. Same as Figure 2 but for models predicting LWP. Scatter plots for the five stratocumulus regions (**a–e**) showing the effect of changes in N_d on LWP using SHAP values. Each dot represents a single observation. The PF for each observation is indicated by color increasing from blue to red. The interconnected dots show the median N_d–SHAP value for 20 equal sample bins across N_d for the 1st (blue) and 4th (red) PF quartiles with one standard deviation indicated by the shaded areas. Shown in grey at the bottom of each panel is a histogram of the distribution of observed N_d.

All regions show a higher sensitivity of LWP to changes in N_d for precipitating clouds (upper quartile of PF, red dots) when compared to non-precipitating clouds (lower quartile of PF, blue dots). This difference is most pronounced for the Californian and Peruvian regions (Figure 5b,e) and is driven by the opposing interaction effects of PF in precipitating and non-precipitating clouds (Figure 6). In all five regions these interaction effects lead to an increase in the predicted LWP with increasing N_d in precipitating clouds (red dots), while non-precipitating clouds (blue dots) are characterized by a decrease in the predicted LWP. Using the same definition of pristine and polluted conditions as in Section 3.1, the sensitivity of LWP (S_{LWP}) to changes in N_d is calculated as the difference in the median SHAP value for the polluted bin minus the pristine bin. Similar to Section 3.1, the 1st and 4th quartile of PF are used to asses the impact of PF on the N_d–LWP relationship by calculating the LWP sensitivity for non-precipitating clouds (S_{LWP}^l) and precipitating clouds (S_{LWP}^h). Figure 7 shows S_{LWP} for all regions with color indicating the cloud state (non-precipitating—blue, precipitating—red). All five regions display a positive S_{LWP} with an inter-regional average of 12 gm^{-2} more liquid water in polluted clouds when compared to pristine conditions. This relationship is further enhanced in precipitating clouds with an average S_{LWP}^h of 15 gm^{-2} and weakened under non-precipitating conditions (S_{LWP}^l = 8 gm^{-2}). While the impact of PF on the N_d–LWP relationship can be observed in all regions, it is especially pronounced in the Californian (S_{LWP}^h = 21 gm^{-2}, S_{LWP}^l = 9 gm^{-2}) and Peruvian (S_{LWP}^h = 15 gm^{-2}, S_{LWP}^l = 7 gm^{-2}) regions.
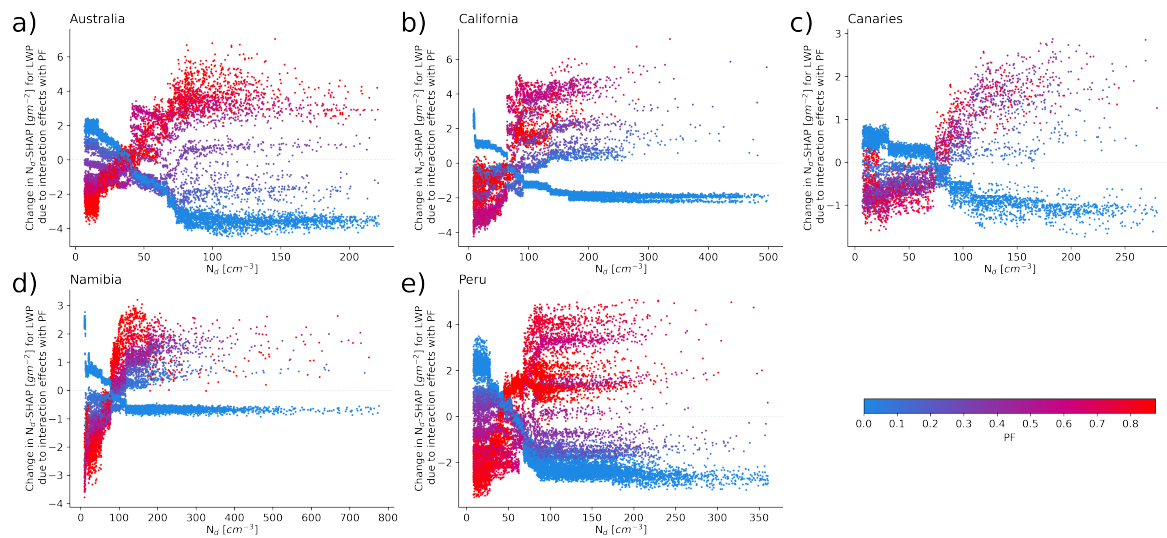
Figure 6. Same as Figure 3 but for models predicting LWP. Scatter plots for the five stratocumulus regions (**a**–**e**) showing the interaction effects for N_d and PF when predicting LWP. Each dot represents a single observation. The PF is indicated by color increasing from blue to red.
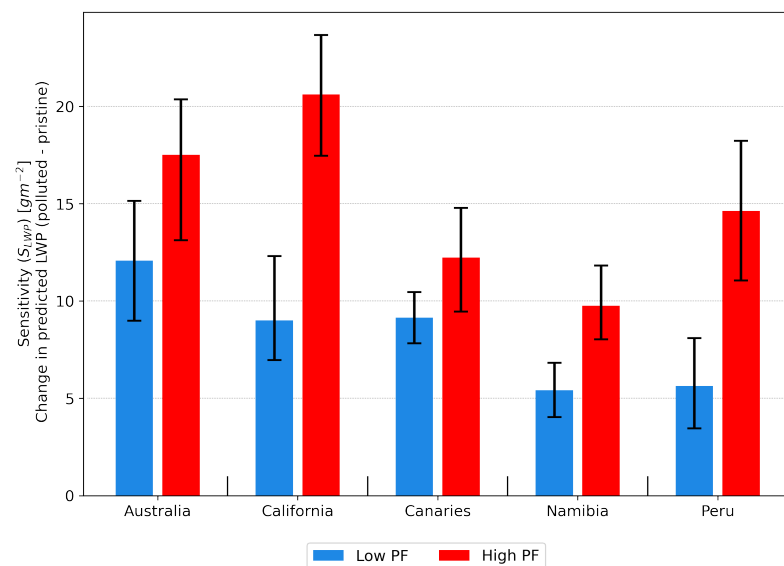

Figure 7. Same as Figure 4 but for models predicting LWP. Sensitivity of LWP (S_{LWP}) to changes in N_d defined as the difference in the bin median Nd-SHAP values between the $20 < N_d < 50$ and $150 < N_d < 250$ bins. Error bars show the range of the differences between the 25th and the 75th percentile of both N_d bins. Values are shown for both low PF (S^l_{LWP}, blue) and high PF (S^h_{LWP}, red) conditions.

4. Discussion

Previous studies examining the relationship between cloud N_d and precipitation often utilize a measure of precipitation susceptibility defined as the negative fractional change in precipitation with a fractional increase in N_d first introduced by Feingold and Siebert [43]. Precipitation susceptibility may be based on different proxies for precipitation, such as the rain rate, the probability of rain, and the rain intensity [44]. Here, we compare the findings of the precipitation susceptibility based on the probability of rain (R_0) to S_{PF} based on PF. The probability of rain as defined in Wang et al. [45] lends itself to comparison with PF as both measures are calculated by relating the number of precipitating clouds to the total number of clouds observed. R_0 is found to be variable in strength depending on the cloud thickness (H) [46,47], but is reported to be strictly positive for MSC in previous

works [44,46–48] when considering the LWP range covered by the dataset analyzed here. A positive R_0 indicates a decrease in the probability of rain with increasing N_d [43], which is in agreement with the findings for S_{PF} presented here. The influence of LWP on R_0 is not described as unambiguously in the literature. While Terai et al. [44,46] suggested a decreasing R_0 in MSC with increasing H, Jung et al. [47] showed that there is an increase in R_0 with increasing H in MSC up to intermediately thick clouds and Gupta et al. [14] reported an overall increase in R_0 with increasing H especially in high N_d environments. An increase in R_0 with H agrees well with the finding of a more negative S_{PF} in high LWP MSC, as both indicate a stronger decrease in the occurrence frequency of precipitation with increasing N_d in clouds with more liquid water available.

Recent studies looking to analyze the N_d–LWP relationship globally based on MODIS satellite obseravtions find a positive sensitivity at low N_d and a negative sensitivity at higher N_d ($N_d > 30$), the latter of which dominates the overall correlation, leading to a decrease of LWP with increasing N_d [8,25]. In contrast to this, a general pattern of LWP increasing with N_d has been reported in previous studies based on models [22,49–51] as well as observation data [23,52,53], which is consistent with the findings of a positive but non-linear N_d–LWP relationship here. Only the Californian and Peruvian stratocumulus regions show a slight decrease in LWP under high N_d conditions in non-precipitating clouds, which may be attributed to the influence of evaporation–entrainment feedback, especially since the two regions show a low average for the relative humidity above cloud (California avg. $RH_{ac} = 29\%$, Peru avg. $RH_{ac} = 20\%$). However, as opposed to the findings of Gryspeerdt et al. [8], this decrease only occurs above a higher N_d threshold ($N_d > 150$), is much smaller in magnitude, and is unable to reverse the overall positive N_d–LWP relationship. The findings here are closer to those displayed in Ackerman et al. [17], who used large eddy simulations that indicate an LWP increase with increasing N_d up to $\approx$60–100 cm^{-3}, depending on the relative humidity above cloud. At this point precipitation may be mostly suppressed, which could then lead to the negative impact of evaporation entrainment on LWP becoming dominant, especially under conditions with drier air above the clouds.

The observation of a decreasing PF (especially for high LWP clouds) with increasing N_d along with an increasing LWP (especially in drizzling clouds) shown here can be explained by the process of precipitation suppression [11]. Clouds characterized by higher LWP that are precipitating or have the potential to develop precipitation are more susceptible to precipitation suppression. However, low LWP clouds are unable to form precipitation due to LWP acting as the limiting factor and hence there can be no precipitation suppression. This tendency of LWP enabling precipitation and N_d regulating precipitation has also been described by Lu et al. [54] albeit in a more general manner for a larger range of LWP than is observed in MSC.

5. Conclusions

In this study, explainable machine learning models (in the form of GBRTs) were trained to predict PF and LWP over five marine areas characterized by a high occurrence of MSC. SHAP values were used to analyze the statistical relationship between N_d, PF, and LWP in order to provide a better understanding of cloud adjustments to aerosol perturbations. The main findings are as follows:

- The GBRT models are able to explain ∼60–70% of the variability (Table 1) in LWP and PF in the five regions considered here.
- With increasing N_d, an overall decrease in PF and increase in LWP is found in all five regions. The decrease in PF is amplified in high LWP clouds and the increase in LWP is stronger for precipitating clouds.
- The process of precipitation suppression is likely responsible for the observed sensitivity of PF and LWP to changes in N_d.

- Evaporation–entrainment feedback may be responsible for a decrease in LWP in non-precipitating clouds under high N_d conditions in the Californian and Peruvian region.

The machine learning framework applied in this work explicitly considers the entire N_d–PF-LWP system and related environmental parameters on a fine spatial scale, thereby yielding more dependable results compared to approaches considering only the binary relationship between cloud parameters. However, even the comparatively high spatial resolution of the dataset used here is still too coarse to resolve processes on the cloud formation scale. In order to further improve the models' performance, an increased spatial resolution for the input data—especially the thermo-dynamic parameters derived from ERA5—would be desirable. Nevertheless, it was possible to demonstrate that the displayed approach is capable of isolating individual processes and is able to account for non-linearity, while also incorporating interactive effects between multiple parameters. Accordingly, the findings discussed in this work show the importance of precipitation suppression in MSC in particular and the potential benefit of utilizing explainable machine learning to analyze ACI. By isolating the impact of individual parameters from other confounding factors—which proved to be a challenging endeavour in previous work—the displayed approach opens an avenue to further disentangle the effects of ACI using models or satellite observations.

Author Contributions: Conceptualization, L.Z. and H.A.; methodology, L.Z. and H.A.; software, L.Z.; formal analysis, L.Z.; writing—original draft preparation, L.Z.; writing—review and editing, H.A., D.P.G. and J.C.; visualization, L.Z.; funding acquisition, H.A. and J.C. All authors have read and agreed to the published version of the manuscript.

Institutional Review Board Statement: Not applicable.

Informed Consent Statement: Not applicable.

Data Availability Statement: Publicly available datasets were analyzed in this study. The C3M dataset can be found at the NASA Langley Research Center: https://doi.org/10.5067/AQUA/CERES/NEWS_CCCM-FM3-MODIS-CAL-CS_L2.RELB1 (accessed on: 12 February 2020). ERA5 data on single levels and on pressure levels are available at the Copernicus Climate Change Service (C3S) Climate Date Store: Single levels—https://doi.org/10.24381/cds.adbb2d47 (accessed on: 8 March 2021), Pressure levels—https://doi.org/10.24381/cds.bd0915c6 (accessed on: 8 March 2021). The AMSR-E dataset is available at the NASA National Snow and Ice Data Center: https://doi.org/10.5067/AMSR-E/AE_RAIN.003 (accessed on: 25 September 2021).

Conflicts of Interest: The authors declare no conflicts of interest.

References

1. Wood, R. Stratocumulus clouds. *Mon. Weather Rev.* **2012**, *140*, 2373–2423. [CrossRef]
2. Latham, J.; Rasch, P.; Chen, C.C.; Kettles, L.; Gadian, A.; Gettelman, A.; Morrison, H.; Bower, K.; Choularton, T. Global temperature stabilization via controlled albedo enhancement of low-level maritime clouds. *Philos. Trans. R. Soc. A Math. Phys. Eng. Sci.* **2008**, *366*, 3969–3987. [CrossRef] [PubMed]
3. Chen, Y.C.; Christensen, M.W.; Stephens, G.L.; Seinfeld, J.H. Satellite-based estimate of global aerosol–cloud radiative forcing by marine warm clouds. *Nat. Geosci.* **2014**, *7*, 643. [CrossRef]
4. Boucher, O.; Randall, D.; Artaxo, P.; Bretherton, C.; Feingold, G.; Forster, P.; Kerminen, V.M.; Kondo, Y.; Liao, H.; Lohmann, U.; et al. Clouds and aerosols. In *Climate Change 2013: The Physical Science Basis. Contribution of Working Group I to the Fifth Assessment Report of the Intergovernmental Panel on Climate Change*; Cambridge University Press: Cambridge, UK, 2013; pp. 571–657. [CrossRef]
5. Zelinka, M.D.; Andrews, T.; Forster, P.M.; Taylor, K.E. Quantifying components of aerosol-cloud-radiation interactions in climate models. *J. Geophys. Res. Atmos.* **2014**, *119*, 7599–7615. [CrossRef]

6. Heyn, I.; Block, K.; Mülmenstädt, J.; Gryspeerdt, E.; Kühne, P.; Salzmann, M.; Quaas, J. Assessment of simulated aerosol effective radiative forcings in the terrestrial spectrum. *Geophys. Res. Lett.* **2017**, *44*, 1001–1007. [CrossRef]

7. Twomey, S. Pollution and the planetary albedo. *Atmos. Environ. (1967)* **1974**, *8*, 1251–1256. [CrossRef]

8. Gryspeerdt, E.; Goren, T.; Sourdeval, O.; Quaas, J.; Mülmenstädt, J.; Dipu, S.; Unglaub, C.; Gettelman, A.; Christensen, M. Constraining the aerosol influence on cloud liquid water path. *Atmos. Chem. Phys.* **2019**, *19*, 5331–5347. [CrossRef]

9. Toll, V.; Christensen, M.; Quaas, J.; Bellouin, N. Weak average liquid-cloud-water response to anthropogenic aerosols. *Nature* **2019**, *572*, 51–55. [CrossRef]

10. Morrison, H.; Gettelman, A. A New Two-Moment Bulk Stratiform Cloud Microphysics Scheme in the Community Atmosphere Model, Version 3 (CAM3). Part I: Description and Numerical Tests. *J. Clim.* **2008**, *21*, 3642–3659. [CrossRef]

11. Albrecht, B.A. Aerosols, cloud microphysics, and fractional cloudiness. *Science* **1989**, *245*, 1227–1230. [CrossRef]

12. Stevens, B.; Cotton, W.R.; Feingold, G.; Moeng, C.H. Large-Eddy Simulations of Strongly Precipitating, Shallow, Stratocumulus-Topped Boundary Layers. *J. Atmos. Sci.* **1998**, *55*, 3616–3638. [CrossRef]

13. Malavelle, F.F.; Haywood, J.M.; Jones, A.; Gettelman, A.; Clarisse, L.; Bauduin, S.; Allan, R.P.; Karset, I.H.H.; Kristjánsson, J.E.; Oreopoulos, L.; et al. Strong constraints on aerosol-cloud interactions from volcanic eruptions. *Nature* **2017**, *546*, 485–491. [CrossRef] [PubMed]

14. Gupta, S.; McFarquhar, G.M.; O'Brien, J.R.; Poellot, M.R.; Delene, D.J.; Miller, R.M.; Small Griswold, J.D. Factors affecting precipitation formation and precipitation susceptibility of marine stratocumulus with variable above- and below-cloud aerosol concentrations over the Southeast Atlantic. *Atmos. Chem. Phys.* **2022**, *22*, 2769–2793. [CrossRef]

15. Haywood, J.M.; Abel, S.J.; Barrett, P.A.; Bellouin, N.; Blyth, A.; Bower, K.N.; Brooks, M.; Carslaw, K.; Che, H.; Coe, H.; et al. The CLoud–Aerosol–Radiation Interaction and Forcing: Year 2017 (CLARIFY-2017) measurement campaign. *Atmos. Chem. Phys.* **2021**, *21*, 1049–1084. [CrossRef]

16. Redemann, J.; Wood, R.; Zuidema, P.; Doherty, S.J.; Luna, B.; LeBlanc, S.E.; Diamond, M.S.; Shinozuka, Y.; Chang, I.Y.; Ueyama, R.; et al. An overview of the ORACLES (ObseRvations of Aerosols above CLouds and their intEractionS) project: Aerosol–cloud–radiation interactions in the southeast Atlantic basin. *Atmos. Chem. Phys.* **2021**, *21*, 1507–1563. [CrossRef]

17. Ackerman, A.S.; Kirkpatrick, M.P.; Stevens, D.E.; Toon, O.B. The impact of humidity above stratiform clouds on indirect aerosol climate forcing. *Nature* **2004**, *432*, 1014–1017. [CrossRef] [PubMed]

18. Bretherton, C.S.; Blossey, P.N.; Uchida, J. Cloud droplet sedimentation, entrainment efficiency, and subtropical stratocumulus albedo. *Geophys. Res. Lett.* **2007**, *34*, L03813. [CrossRef]

19. Wang, S.; Wang, Q.; Feingold, G. Turbulence, Condensation, and Liquid Water Transport in Numerically Simulated Nonprecipitating Stratocumulus Clouds. *J. Atmos. Sci.* **2003**, *60*, 262–278. [CrossRef]

20. Small, J.D.; Chuang, P.Y.; Feingold, G.; Jiang, H. Can aerosol decrease cloud lifetime? *Geophys. Res. Lett.* **2009**, *36*, L16806. [CrossRef]

21. Dagan, G.; Koren, I.; Altaratz, O.; Heiblum, R.H. Time-dependent, non-monotonic response of warm convective cloud fields to changes in aerosol loading. *Atmos. Chem. Phys.* **2017**, *17*, 7435–7444. [CrossRef]

22. Neubauer, D.; Christensen, M.W.; Poulsen, C.A.; Lohmann, U. Unveiling aerosol–cloud interactions—Part 2: Minimising the effects of aerosol swelling and wet scavenging in ECHAM6-HAM2 for comparison to satellite data. *Atmos. Chem. Phys.* **2017**, *17*, 13165–13185. [CrossRef]

23. Zipfel, L.; Andersen, H.; Cermak, J. Machine-Learning Based Analysis of Liquid Water Path Adjustments to Aerosol Perturbations in Marine Boundary Layer Clouds Using Satellite Observations. *Atmosphere* **2022**, *13*, 586. [CrossRef]

24. Rosenfeld, D.; Zhu, Y.; Wang, M.; Zheng, Y.; Goren, T.; Yu, S. Aerosol-driven droplet concentrations dominate coverage and water of oceanic low-level clouds. *Science* **2019**, *363*, 6427. [CrossRef] [PubMed]

25. Gryspeerdt, E.; Glassmeier, F.; Feingold, G.; Hoffmann, F.; Murray-Watson, R.J. Observing short-timescale cloud development to constrain aerosol–cloud interactions. *Atmos. Chem. Phys.* **2022**, *22*, 11727–11738. [CrossRef]

26. Klein, S.A.; Hartmann, D.L. The Seasonal Cycle of Low Stratiform Clouds. *J. Clim.* **1993**, *6*, 1587–1606. [CrossRef]

27. Kato, S.; Rose, F.G.; Sun-Mack, S.; Miller, W.F.; Chen, Y.; Rutan, D.A.; Stephens, G.L.; Loeb, N.G.; Minnis, P.; Wielicki, B.A.; et al. Improvements of top-of-atmosphere and surface irradiance computations with CALIPSO-, CloudSat-, and MODIS-derived cloud and aerosol properties. *J. Geophys. Res. Atmos.* **2011**, *116*, D19209. [CrossRef]

28. Adebiyi, A.A.; Zuidema, P.; Chang, I.; Burton, S.P.; Cairns, B. Mid-level clouds are frequent above the southeast Atlantic stratocumulus clouds. *Atmos. Chem. Phys.* **2020**, *20*, 11025–11043. [CrossRef]

29. Grosvenor, D.P.; Sourdeval, O.; Zuidema, P.; Ackerman, A.; Alexandrov, M.D.; Bennartz, R.; Boers, R.; Cairns, B.; Chiu, J.C.; Christensen, M.; et al. Remote Sensing of Droplet Number Concentration in Warm Clouds: A Review of the Current State of Knowledge and Perspectives. *Rev. Geophys.* **2018**, *56*, 409–453. [CrossRef]

30. Quaas, J.; Boucher, O.; Lohmann, U. Constraining the total aerosol indirect effect in the LMDZ and ECHAM4 GCMs using MODIS satellite data. *Atmos. Chem. Phys.* **2006**, *6*, 947–955. [CrossRef]

31. Hersbach, H.; Bell, B.; Berrisford, P.; Biavati, G.; Horányi, A.; Muñoz-Sabater, J.; Nicolas, J.; Peubey, C.; Radu, R.; Rozum, I.; et al. ERA5 hourly data on single levels from 1979 to present. In *Copernicus Climate Change Service (C3S) Climate Data Store (CDS)*; European Union: Brussels, Belgium, 2018. [CrossRef]

32. Hersbach, H.; Bell, B.; Berrisford, P.; Biavati, G.; Horányi, A.; Muñoz-Sabater, J.; Nicolas, J.; Peubey, C.; Radu, R.; Rozum, I.; et al. ERA5 hourly data on pressure levels from 1979 to present. In *Copernicus Climate Change Service (C3S) Climate Data Store (CDS)*; European Union: Brussels, Belgium, 2018. [CrossRef]

33. Wood, R.; Bretherton, C.S. On the relationship between stratiform low cloud cover and lower-tropospheric stability. *J. Clim.* **2006**, *19*, 6425–6432. [CrossRef]

34. Kummerow, C.; Ferraro, R.; Randel, D. *AMSR-E/Aqua L2B Global Swath Surface Precipitation GSFC Profiling Algorithm, Version 3*; NASA National Snow and Ice Data Center Distributed Active Archive Center: Boulder, CO, USA, 2015. [CrossRef]

35. Elith, J.; Leathwick, J.R.; Hastie, T. A working guide to boosted regression trees. *J. Anim. Ecol.* **2008**, *77*, 802–813. [CrossRef] [PubMed]

36. Fuchs, J.; Cermak, J.; Andersen, H. Building a cloud in the southeast Atlantic: Understanding low-cloud controls based on satellite observations with machine learning. *Atmos. Chem. Phys.* **2018**, *18*, 16537–16552. [CrossRef]

37. Dadashazar, H.; Crosbie, E.; Majdi, M.S.; Panahi, M.; Moghaddam, M.A.; Behrangi, A.; Brunke, M.; Zeng, X.; Jonsson, H.H.; Sorooshian, A. Stratocumulus cloud clearings: Statistics from satellites, reanalysis models, and airborne measurements. *Atmos. Chem. Phys.* **2020**, *20*, 4637–4665. [CrossRef] [PubMed]

38. Andersen, H.; Cermak, J.; Zipfel, L.; Myers, T.A. Attribution of Observed Recent Decrease in Low Clouds Over the Northeastern Pacific to Cloud-Controlling Factors. *Geophys. Res. Lett.* **2022**, *49*, e2021GL096498. [CrossRef]

39. Jia, Y.; Andersen, H.; Cermak, J. Analysis of cloud fraction adjustment to aerosols and its dependence on meteorological controls using explainable machine learning. *EGUsphere* **2023**, *2023*, 1–25. [CrossRef]

40. Eastman, R.; McCoy, I.L.; Wood, R. Environmental and Internal Controls on Lagrangian Transitions from Closed Cell Mesoscale Cellular Convection over Subtropical Oceans. *J. Atmos. Sci.* **2021**, *78*, 2367–2383. [CrossRef]

41. Lundberg, S.M.; Lee, S.I. A Unified Approach to Interpreting Model Predictions. In *Advances in Neural Information Processing Systems 30*; Guyon, I., Luxburg, U.V., Bengio, S., Wallach, H., Fergus, R., Vishwanathan, S., Garnett, R., Eds.; Curran Associates, Inc.: Glasgow, UK, 2017; pp. 4765–4774.

42. Lundberg, S.M.; Erion, G.; Chen, H.; DeGrave, A.; Prutkin, J.M.; Nair, B.; Katz, R.; Himmelfarb, J.; Bansal, N.; Lee, S.I. From local explanations to global understanding with explainable AI for trees. *Nat. Mach. Intell.* **2020**, *2*, 56–67. [CrossRef]

43. Feingold, G.; Siebert, H. Cloud—Aerosol Interactions from the Micro to the Cloud Scale. In *Clouds in the Perturbed Climate System: Their Relationship to Energy Balance, Atmospheric Dynamics, and Precipitation*; MIT Press: Cambridge, MA, USA, 2009; pp. 319–338.

44. Terai, C.R.; Wood, R.; Kubar, T.L. Satellite estimates of precipitation susceptibility in low-level marine stratiform clouds. *J. Geophys. Res. Atmos.* **2015**, *120*, 8878–8889. [CrossRef]

45. Wang, M.; Ghan, S.; Liu, X.; L'Ecuyer, T.S.; Zhang, K.; Morrison, H.; Ovchinnikov, M.; Easter, R.; Marchand, R.; Chand, D.; et al. Constraining cloud lifetime effects of aerosols using A-Train satellite observations. *Geophys. Res. Lett.* **2012**, *39*, 15. [CrossRef]

46. Terai, C.R.; Wood, R.; Leon, D.C.; Zuidema, P. Does precipitation susceptibility vary with increasing cloud thickness in marine stratocumulus? *Atmos. Chem. Phys.* **2012**, *12*, 4567–4583. [CrossRef]

47. Jung, E.; Albrecht, B.A.; Sorooshian, A.; Zuidema, P.; Jonsson, H.H. Precipitation susceptibility in marine stratocumulus and shallow cumulus from airborne measurements. *Atmos. Chem. Phys.* **2016**, *16*, 11395–11413. [CrossRef]

48. Bai, H.; Gong, C.; Wang, M.; Zhang, Z.; L'Ecuyer, T. Estimating precipitation susceptibility in warm marine clouds using multi-sensor aerosol and cloud products from A-Train satellites. *Atmos. Chem. Phys.* **2018**, *18*, 1763–1783. [CrossRef]

49. Quaas, J.; Ming, Y.; Menon, S.; Takemura, T.; Wang, M.; Penner, J.E.; Gettelman, A.; Lohmann, U.; Bellouin, N.; Boucher, O.; et al. Aerosol indirect effects – general circulation model intercomparison and evaluation with satellite data. *Atmos. Chem. Phys.* **2009**, *9*, 8697–8717. [CrossRef]

50. Grosvenor, D.P.; Field, P.R.; Hill, A.A.; Shipway, B.J. The relative importance of macrophysical and cloud albedo changes for aerosol-induced radiative effects in closed-cell stratocumulus: Insight from the modelling of a case study. *Atmos. Chem. Phys.* **2017**, *17*, 5155–5183. [CrossRef]

51. McCoy, D.T.; Field, P.R.; Schmidt, A.; Grosvenor, D.P.; Bender, F.A.M.; Shipway, B.J.; Hill, A.A.; Wilkinson, J.M.; Elsaesser, G.S. Aerosol midlatitude cyclone indirect effects in observations and high-resolution simulations. *Atmos. Chem. Phys.* **2018**, *18*, 5821–5846. [CrossRef]

52. Koren, I.; Dagan, G.; Altaratz, O. From aerosol-limited to invigoration of warm convective clouds. *Science* **2014**, *344*, 1143–1146. [CrossRef] [PubMed]

53. Gryspeerdt, E.; Stier, P.; Partridge, D.G. Satellite observations of cloud regime development: The role of aerosol processes. *Atmos. Chem. Phys.* **2014**, *14*, 1141–1158. [CrossRef]

54. Lu, M.L.; Sorooshian, A.; Jonsson, H.H.; Feingold, G.; Flagan, R.C.; Seinfeld, J.H. Marine stratocumulus aerosol-cloud relationships in the MASE-II experiment: Precipitation susceptibility in eastern Pacific marine stratocumulus. *J. Geophys. Res. Atmos.* **2009**, *114*, D24. [CrossRef]